Kinematics and control of redundant robotic arm based on Dielectric Elastomer Actuators

Francesco Branz[a], Andrea Antonello[a], Andrea Carron[b], Ruggero Carli[b] and Alessandro Francesconi[c]

[a] CISAS "G. Colombo", University of Padova, Italy;
[b] Department of Information Engineering, University of Padova, Italy;
[c] Department of Industrial Engineering, University of Padova, Italy

ABSTRACT

Soft robotics is a promising field and its application to space mechanisms could represent a breakthrough in space technologies by enabling new operative scenarios (e.g. soft manipulators, capture systems). Dielectric Elastomers Actuators have been under deep study for a number of years and have shown several advantages that could be of key importance for space applications. Among such advantages the most notable are high conversion efficiency, distributed actuation, self-sensing capability, multi-degree-of-freedom design, light weight and low cost. The big potentialities of double cone actuators have been proven in terms of good performances (i.e. stroke and force/torque), ease of manufacturing and durability. In this work the kinematic, dynamic and control design of a two-joint redundant robotic arm is presented. Two double cone actuators are assembled in series to form a two-link design. Each joint has two degrees of freedom (one rotational and one translational) for a total of four. The arm is designed to move in a 2-D environment (i.e. the horizontal plane) with 4 DoF, consequently having two degrees of redundancy. The redundancy is exploited in order to minimize the joint loads. The kinematic design with redundant Jacobian inversion is presented. The selected control algorithm is described along with the results of a number of dynamic simulations that have been executed for performance verification. Finally, an experimental setup is presented based on a flexible structure that counteracts gravity during testing in order to better emulate future zero-gravity applications.

Keywords: Dielectric Elastomer actuators, soft robotics, space robotics, smart materials, Electroactive Polymers

1. INTRODUCTION

Research in robotics focused recently on the use of new approaches aiming to expand the field of application of existing systems. Soft robotics studies the possibility to exploit deformable materials or control algorithms to obtain innovative systems with improved operational flexibility. Compared to traditional robotics, in which the manipulators are composed by rigid links and position-controlled joints, a major advantage of soft robotics is the compliance to external environment which allows a safer interaction with brittle targets or humans, and eases the operation in an unpredicted environment. This quality can be achieved by means of sophisticated control systems or by implementing robots based on soft materials and structures[1]. A large number of actuator solutions based on smart materials (i.e. shape memory alloys and polymers, piezoelectric crystals and polymers, etc.) have been proposed recently, many of them being inspired by biological systems[2]; in particular, several solutions exploit the capabilities of Electro-Active Polymers (EAP)[3] and, more specifically, of the promising Dielectric Elastomers (DE)[4]. Some space applications of smart materials at different levels of technology readiness exist[5 6 7 8].

Robotic systems in space are widely exploited and under continuous development. Multi-DoF robotic arms have become more and more appealing in recent years as they represent a viable and cost effective alternative to human crew for On Orbit Servicing (OOS) missions. Such missions require the manipulation of both cooperative and uncooperative

---

Further author information: (Send correspondence to F. B.)

F. B.: e-mail: francesco.branz@studenti.unipd.it, telephone: +39 049 827 6836

A. A.: e-mail: andrea.antonello.it@gmail.com

A. C.: e-mail: andcarron@gmail.com

R. C.: e-mail: carlirug@dei.unipd.it

A. F.: e-mail: alessandro.francesconi@unipd.it

objects for several purposes such as refurbishment, refuelling, re-boosting, repairing or deorbiting[9 10 11]. Nevertheless, to date only a couple of spacecraft have been launched with the aim to demonstrate the capabilities of performing the tasks required by OOS with manipulators (OrbitalExpress[12], ETS-VII[13]) and few other systems have been proposed[14 15].

The implementation of soft robotic systems in a space scenario can provide key abilities for the realization of a variety of missions thanks to their intrinsic adaptability to the target object. The capture and manipulation of an orbital object are complex tasks with a large number of uncertain parameters including mass and dynamic properties of the system. The typical scenario of an OOS mission can be partially unknown since the target objects characteristics can be different from the original at the beginning of operational life (e.g. structural damages, fuel depletion, malfunctioning). In order to safely approach and operate on such vehicles it is necessary to develop tolerant systems that can comply with the actual operative situation. For this reason the development of robust and flexible soft robotics systems can enable several new scenarios, with great potentialities in increasing the efficiency of space exploitation.

The big potentialities of DEs in robotic actuation applications have been proven by several studies[16 17 18 19]. Although their mechanical behavior is not always straightforward (i.e. non-linear elasticity, large deformations, time dependent stress-strain relation), they have shown many interesting characteristics like actuation/generation capabilities[20], manufacturing simplicity, applicability to multiple DoF systems[16], self-sensing functionalities[21].

In this work, the design of an experimental, redundant robotic arm based on double-cone DE actuators is presented. The actuators model adopted is briefly described in Sec. 2, while the manipulator configuration is explained in Sec. 3. The approach used for the resolution of redundancy and for controlling the system are presented in Sec. 4 and Sec. 5. In Sec. 6 the dynamic simulation results are discussed and in Sec. 7 the test setup that will be used for evaluating the manipulator performances is described.

2. ACTUATOR MODEL

The selected actuator design for the proposed robotic arm is the double-cone actuator. The choice of this device was based on the multi-DoF capabilities, the large maximum deformations and the manufacturing simplicity. The configuration adopted provides two DoF in the plane, one rotational and one translational. The modelling of torque/force and rotation/stroke performances of the device has been under deep study by the authors at CISAS "G. Colombo", University of Padova, over the last years[22]. The results of such activity are exploited in the manipulator design and presented here briefly. The strong non-linearities typical of DE devices determine non-negligible model uncertainties that are quantitatively reported in the following.

DE elastomer devices exploit the deformation achievable in elastomeric membranes by means of applied high voltage (HV). The chosen material is an acrylic elastomer called 3M™VHB™49XX. In the case of double cone actuators, two circular elastomer membranes are radially pre-stretched, deformed to a cone-like shape and mounted concentric, one

(a) Actuator prototype   (b) Side view schematics
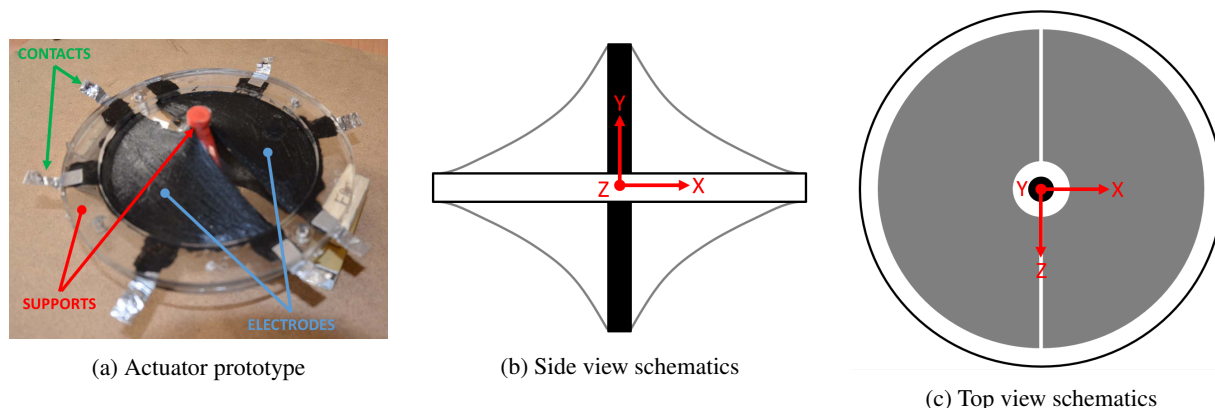
(c) Top view schematics

Figure 1: Actuator prototype picture (a) with specification of main components (electrodes, contacts, supports); side (b) and top view (c) schematics of the actuator geometry showing circular membranes with electrodes (grey), support ring (white w/ black contour) and rigid rod (black). The main reference system is shown.

mirrored to the other (see Fig. 1). Rigid rings and rods are used to keep the deformable elements in position. The elastomer elements can be, in general, composed by a multilayer stack of polymer sheets.

The rigid components of the actuator (circular frames and central rod) are made of a non-conductive, hard polymeric material like acrylonitrile butadiene styrene (ABS) or poly(methyl methacrylate) (PMMA). Compliant electrodes are applied on the upper and lower surface of each elastomer layer. Such electrodes are obtained by applying conductive carbon grease. Two conductive regions are obtained this way on each circular surface; they are half circular shaped, insulated from each other. By differentially applying the voltage to the electrode regions it is possible to actuate either one or the other degree of freedom. Fig. 2a shows all the possible combinations of electrode activation (valid for both single- and multi-layer membrane design): the rotation, θ, about the Z-axis and the translation, y, along the Y-axis are allowed. In the proposed multilayer configuration the electrodes have to be manufactured on both sides of each layer and the high voltage has to be applied across each layer.

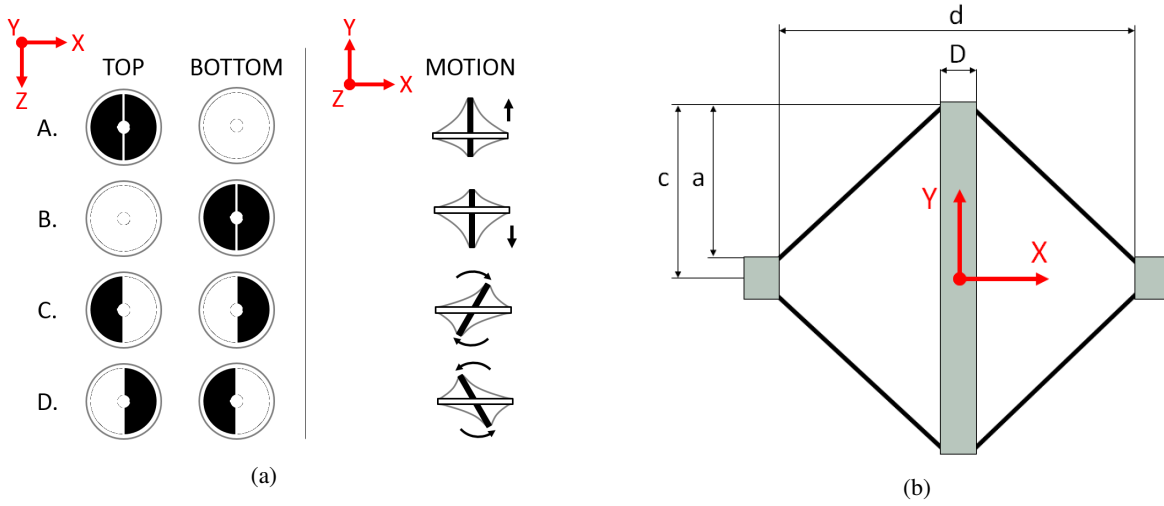(a)   (b)

Figure 2: (2a) Actuation of the considered DoFs: the electrodes are half circular, black if high voltage is on, white if high voltage is off. Voltage loads on the top and bottom membrane are shown in the first two columns, while the third one shows the motion triggered by the actuation. The four rows list the possible motions: +Y and -Y translation, +Z and -Z rotation. (2b) Schematic section view of the actuator with main geometric parameters (Z-axis points at the reader).

Parametric relations for the estimation of the steady state values of blocking force/torque (F and T) and stroke/rotation (y and θ) with no load as a function of applied voltage, V, have been obtained and are presented in concise form in Eq. 1. These relations have a mean prediction error around 20%. The parameters in Eq. 1 are geometric parameters of the actuator and most of them are shown in Fig. 2b: d is the membrane external diameter, D is the membrane inner diameter or central rod diameter, a is the amount of out-of-plane displacement imposed to the membranes, c is half of the rod length. Other parameters not shown in Fig. 2b are the unstretched membrane thickness, t, the number of elastomer layers in the membrane, n, and the stretch ratio, λ. For all considerations, computations and simulations presented in this work the following parameters are assumed: $d = 100$ mm, $D = 12$ mm, $a = 23$ mm, $c = 25$ mm, $t = 1$ mm, $n = 1$ and $\lambda = 3.5$.

$$T_{\theta=0} = f_1\left(c,d,D,n,t,\lambda\right) \cdot V^2$$
$$F_{Y=0} = f_2\left(a,d,D,n,t,\lambda\right) \cdot V^2$$
$$\theta_{T=0} = f_3\left(\frac{a}{c},\frac{a}{d},\frac{D}{d},\lambda\right) \cdot V^2$$
$$y_{F=0} = f_4\left(a,d,D,n,t,\lambda\right) \cdot V^2 \tag{1}$$

The value of T and F is a function of θ and y respectively. Eq. 2 shows this relation at a given value of applied voltage, V (it is clear that to hold a given rotation or stroke value it is necessary to apply a continuous voltage).

$$T(\theta)\Big|_V = T_{\theta=0}\Big|_V - k_\theta \cdot \theta$$

$$F(y)\Big|_V = F_{y=0}\Big|_V - k_y \cdot y \tag{2}$$

where $k_\theta = \dfrac{f_1}{f_3}$ and $k_y = \dfrac{f_2}{f_4}$.

The time behavior of the device in terms of Transfer Functions (TF) was estimated through experimental evaluation (mean error on 70% rise time is $\sim 25\%$). Mainly due to the relaxation behavior of the membrane material, the actuator has a highly damped behavior; this is applicable to all actuator outputs (i.e. T, θ and y) except for the blocking force in the Y-axis direction whose TF is unity. The cut-off frequency for both torque/force and rotation/stroke is generally below $\sim$5 rad/s. Assuming to have an ideal power supply, the actuator transfer functions normalized w.r.t. the Bode gain, f_i (Eq. 1), have the form shown in Eq. 3:

$$G_{T_0}(s) = \frac{T}{f_1 V^2} = \frac{n_3^{(T)}s^3 + n_2^{(T)}s^2 + n_1^{(T)}s + 1}{d_4^{(T)}s^4 + d_3^{(T)}s^3 + d_2^{(T)}s^2 + d_1^{(T)}s + 1}$$

$$G_{F_0}(s) = \frac{F}{f_2 V^2} = 1$$

$$G_{\theta_0}(s) = \frac{\theta}{f_3 V^2} = \frac{n_3^{(\theta)}s^3 + n_2^{(\theta)}s^2 + n_1^{(\theta)}s + 1}{d_4^{(\theta)}s^4 + d_3^{(\theta)}s^3 + d_2^{(\theta)}s^2 + d_1^{(\theta)}s + 1}$$

$$G_{y_0}(s) = \frac{y}{f_4 V^2} = \frac{n_2^{(y)}s^2 + n_1^{(y)}s + 1}{d_3^{(y)}s^3 + d_2^{(y)}s^2 + d_1^{(y)}s + 1}$$

$$\tag{3}$$

where $n_i^{(\cdot)}$ and $d_i^{(\cdot)}$ are appropriate numerical coefficients. Note that $G_{\theta_0}(s)$ and $G_{y_0}(s)$ depend on the inertial properties of the actuator and its load.

The models described so far assess the actuator behavior as a single device. In order to implement the actuators inside the simulation model it was necessary to develop a further approximated model derived from the transfer functions in Eq. 3. This model is depicted in Fig. 3 that shows the block diagram (Fig. 3a) and the model accordance with measured response for both rotation (Fig. 3b) and translation (Fig. 3c). In Fig. 3a the actuator model for the rotational degree of freedom is described, but something analogous can be developed for translation. The squared value of input voltage, V^2, becomes the input torque, T, through $G_{T_0}(s)$ and the gain f_1. This torque is summed to a component depending on the rotational velocity, $Q(\dot\theta)$, and becomes the input of the actuator dynamics described by Eq. 4. The function $Q(\dot\theta)$ is estimated considering the responses of $G_{T_0}(s)$ and $G_{\theta_0}(s)$.

$$\dot\theta = \frac{s}{I_a s^2 + c_\theta s + k_\theta} T \tag{4}$$

I_a is the actuator rotor inertia, k_θ describes the elastic behavior, while c_θ is a properly tuned damping coefficient necessary to guarantee stability. The latter has to be introduced artificially in the actuator model and is the main responsible for the model inaccuracies shown in Fig. 3a-3b. The adopted approximation is reasonable for the purpose of this work.

## 3. MANIPULATOR CONFIGURATION AND WORKSPACE

The configuration selected in this work is planar and composed by two actuators mounted in series. This design was chosen aiming to ease the realization of a laboratory experiment with simulated zero-gravity conditions. The manipulator has four Joint Variables (JV), while the end-effector has three DoF (X and Y position, orientation) two of whom are controlled
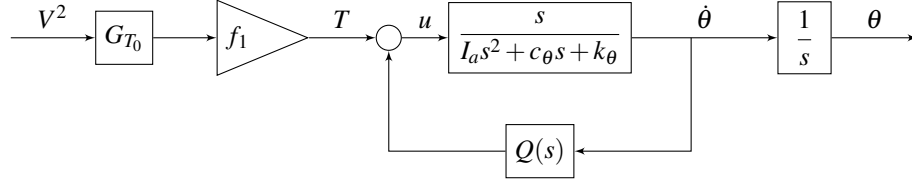
(a) Block diagram used in simulations for the approximate modeling of the actuator.
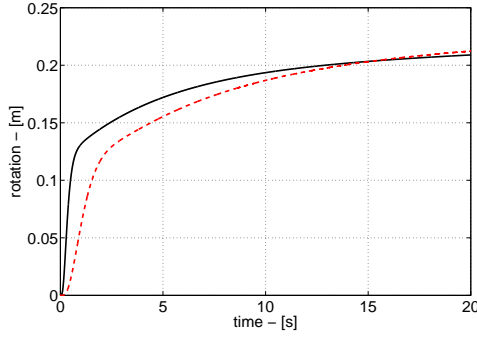
(b) Rotational response to 10 mNm commanded input: comparison between measured (black) and simulated response (red dashed).
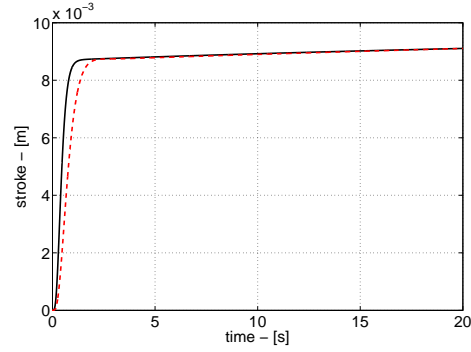
(c) Stroke response to 1 N commanded input: comparison between measured (black) and simulated response (red dashed).

Figure 3: Simulation oriented model adopted for the rotational DoF response prediction of a single actuator (translational version is analogous). Some error between response from TF in Eq. 3 and the simulated response is present; the approximation is reasonable for the purpose of this work.
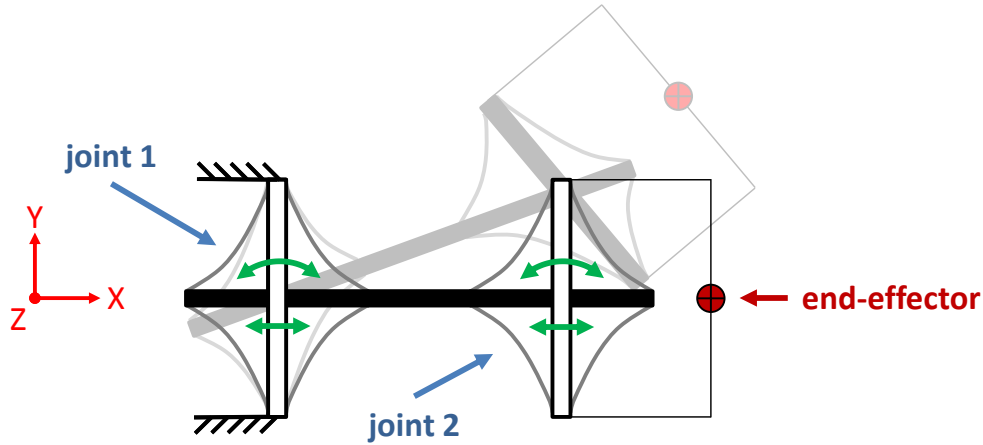

Figure 4: Manipulator architecture: two actuators (joint 1 & 2, blue) with two DoF each (green arrows), with a point end-effector (red).

(position), leading to two degrees of redundancy. The system architecture is shown in Fig. 4. The first actuator is fixed to ground at the outer support ring, while the connection between the two actuators is between the central rods. The end-effector marker is held by a light structure attached to the second actuator outer ring.

The equivalent kinematic model is shown in Fig. 5a. The four joint variables are shown in the picture: two of them are translational (d_1 and d_3), two are rotational (θ_2 and θ_4). The end-effector position is defined by three variables: position (x_e and y_e) and orientation (θ_e). The vector of JV is defined as $\vec{q} = \{d_1\ \theta_2\ d_3\ \theta_4\}^T$, while the vector of end-effector positions is $\vec{x}_e = \{x_e\ y_e\ \theta_e\}^T$. Each actuator allows two degrees of freedom and they are kinematically modeled as two joints (i.e. one translational and one rotoidal) with a fictious link between them. The actuators have intrinsic limitations

on the joint variables: assuming the design parameters specified in Sec. 2 and $V_{max} = 4500$ V, the approximate values of maximum rotation and stroke are $\theta_{max} = \pm 40$ deg and $d_{max} = \pm 5$ mm respectively. Expected blocking force and torque are $F_{max} = 0.5$ N and $T_{max} = 27$ mNm, respectively. The lengths of the manipulator links considered in this work are $b_1 = b_2 = b = 60$ mm. The end-effector workspace is depicted in Fig. 5b: the relatively limited JV range determines a reduced workspace.
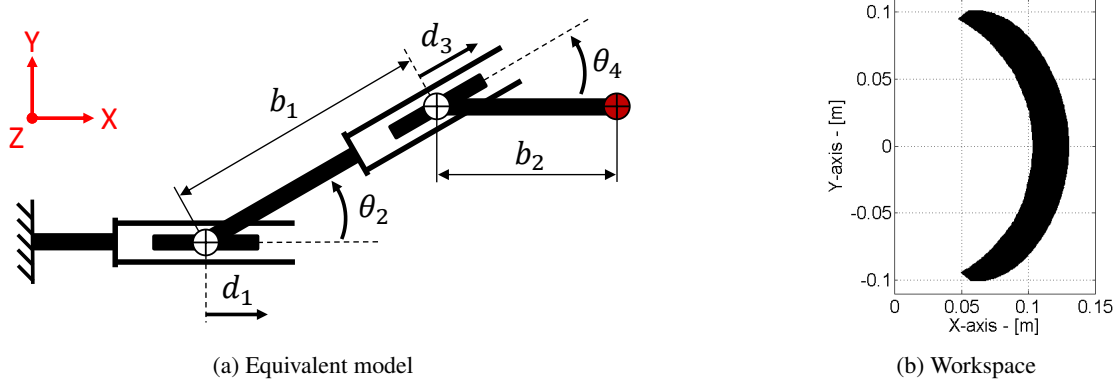

(a) Equivalent model   (b) Workspace

Figure 5: (5a) Equivalent kinematic model of the manipulator with joint variables (d_1, θ_2, d_3 and θ_4) and end-effector (red). (5b) End-effector workspace with mentioned parameters ($\theta_{max} = \pm 40$ deg, $d_{max} = \pm 5$ mm, $b_1 = b_2 = b = 60$ mm).

4. ROBOT KINEMATICS AND DYNAMICS

The robot direct kinematic is obtained by geometrical relations based on Fig. 5a and presented in Eq. 5[23] with $b_1 = b_2 = b$.

$$\vec{x}_e = k(\vec{q}) = \begin{Bmatrix} d_1 + (b+d_3)\cos(\theta_2) + b\cos(\theta_2 + \theta_4) \\ (b+d_3)\sin(\theta_2) + b\sin(\theta_2 + \theta_4) \\ \theta_2 + \theta_4 \end{Bmatrix} \tag{5}$$

Direct partial differentiation of $k(\vec{q})$ with respect to $\vec{q}$ leads to the computation of the analytical Jacobian, $\mathbf{J}_A$, which relates joint velocities, $\dot{\vec{q}}$, and end-effector velocities, $\dot{\vec{x}}_e$ (Eq. 6)[23].

$$\dot{\vec{x}}_e = \mathbf{J}_A \dot{\vec{q}} \quad \text{with} \quad \mathbf{J}_A = \frac{\partial k(\vec{q})}{\partial \vec{q}} \tag{6}$$

The complete Jacobian is a $[3 \times 4]$ matrix. Since a point-to-point trajectory is commanded, the orientation of the end-effector is not taken into account. Consequently, the Jacobian, $\mathbf{J}$, used in simulations is a $[2 \times 4]$ reduced version of $\mathbf{J}_A$ of which only the first two rows are considered. The robot is redundant, thus $\mathbf{J}$ is not a square matrix and, therefore, not invertible.

The system is proposed for space applications in zero-gravity conditions. Other external forces are neglected, leading to the equation of motion shown in Eq. 7 (matrix form)[23].

$$\mathbf{B}(\vec{q})\ddot{\vec{q}} + \mathbf{n}(\vec{q}, \dot{\vec{q}}) = \vec{\tau} \tag{7}$$

where $\mathbf{B}(\vec{q})$ is the robot mass matrix that accounts for all inertial terms, $\mathbf{n}(\vec{q}, \dot{\vec{q}})$ accounts for Coriolis and centrifugal terms and $\vec{\tau}$ is the vector of generalized joint torques.

A commonly used pseudoinverse algorithm is employed for the computation of the inverse kinematics (and dynamics): it is the inertia-weighted version of the Moore-Penrose pseudoinverse and the weight matrix is the robot mass matrix $\mathbf{B}$ (Eq. 8)[24][25].

$$\mathbf{J}_B^\dagger = \mathbf{B}^{-1} \mathbf{J}^T (\mathbf{J}\mathbf{B}^{-1}\mathbf{J}^T)^{-1} \tag{8}$$

where $\mathbf{J}_B^\dagger$ is the pseudoinverse of $\mathbf{J}$. The task space control architecture is selected due to the type of measurement system employed for feedback. At this stage of development self-sensing capabilities of DE actuators are not considered: the position of the end-effector is sensed by a vision system. A torque-based redundancy resolution is selected, since the available actuator model provides output torque/force with related saturation limits (see Sec. 2). The work by Nakanishi *et al.*[25] is exploited for the selection of the control law. Knowing that $(\mathbb{I}_4 - \mathbf{J}_B^\dagger \mathbf{J})$ projects arbitrary vectors onto the null space of the Jacobian, $\mathbf{J}$, it is possible to exploit the dynamical decoupling property of joint torques*: a desired joint torques command is decoupled between those torques that create task space forces and those that act only in the null space of the task. The control law used to compute desired torques is a dynamical decoupling controller with null space pre-multiplication of $\mathbf{B}$ and compensation of $\mathbf{n}$ in joint space (Eq. 9). The arbitrary null space vector is selected to be $\vec{\tau}_0 = \mathbf{B}\ddot{\vec{q}}_0$.

$$\vec{\tau} = \mathbf{B}\left[\mathbf{J}_B^\dagger\left(\ddot{\vec{x}}_r - \dot{\mathbf{J}}\dot{\vec{q}}\right) + \left(\mathbb{I}_4 - \mathbf{J}_B^\dagger \mathbf{J}\right)\ddot{\vec{q}}_0\right] + \mathbf{n} \tag{9}$$

where $\ddot{\vec{x}}_r$ is the reference vector of end-effector acceleration computed from the desired end-effector position, $\vec{x}_d$, velocity, $\dot{\vec{x}}_d$, and acceleration, $\ddot{\vec{x}}_d$, using a proportional/derivative law (PD) as shown in Eq. 10.

$$\ddot{\vec{x}}_r = \ddot{\vec{x}}_d + \mathbf{K}_D\left(\dot{\vec{x}}_d - \dot{\vec{x}}_e\right) + \mathbf{K}_P\left(\vec{x}_d - \vec{x}_e\right) \tag{10}$$

where $\mathbf{K}_P$ and $\mathbf{K}_D$ are proportional and derivative matrix gains respectively. The vector $\ddot{\vec{q}}_0$ is chosen to appropriately exploit the robot redundancy and avoid joint limits (Eq. 11).

$$\ddot{\vec{q}}_0 = -\frac{k_0}{4}\left\{\frac{d_1}{k_d} \quad \frac{\theta_2}{k_\theta} \quad \frac{d_3}{k_d} \quad \frac{\theta_4}{k_\theta}\right\}^T \tag{11}$$

with $k_d = (2d_{max})^2$ and $k_\theta = (2\theta_{max})^2$ and k_0 is an appropriate scalar gain. This choice of the null vector tends to minimize the value of each joint variable without affecting the task space.

The torques computed with Eq. 9 are used as inputs to the *gaussian regression* algorithm as explained in Sec. 5.

5. CONTROL ALGORITHM

The manipulator system model is tested with a trajectory tracking task: to achieve this goal, two control schemes are presented. The first is based on a classic PD controller described in Eq. 10 (Fig. 6), where the parameters are manually tuned, while the second is based on a feedforward compensator (Fig. 7), in which the inverse dynamics is estimated using *gaussian regression*. The latter will be explained in the following.
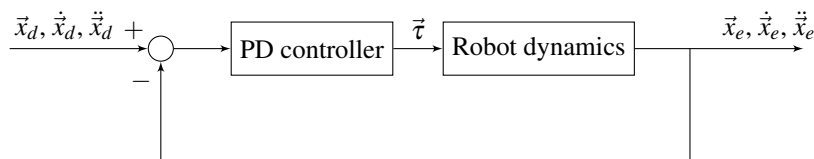

Figure 6: Block schematics of system controlled with the PD scheme.

Feedforward is based on the knowledge of the inverse dynamics of the system that allows to calculate the torques needed to reach a given robot configuration. With this approach it is possible to directly drive the manipulator from an initial to a final end-effector position. In order to overcome robustness issues in the feedforward scheme, it is good practice to close the loop with a low-gain PD controller to reject possible disturbances. A key point in this control scheme is the knowledge of the inverse dynamics. In this work the dynamics is inverted with the procedure described in Sec. 4 that provides one of the infinite solutions to the redundant problem. Although the inverse dynamics is known, the model is affected by non-negligible inaccuracies compared to the real system (see Sec. 2) mainly due to the difficulties in modeling

---

*the symbol $\mathbb{I}_i$ denotes the identity matrix of size $i \times i$
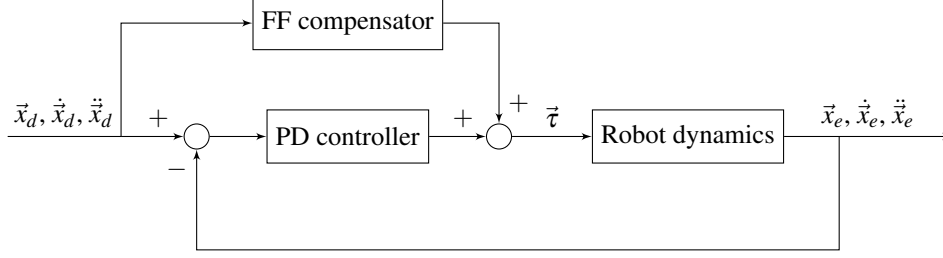
Figure 7: Block schematics of system controlled with the feedforward and PD scheme.

the highly non-linear DE actuators. A way to improve the performances of the feedforward algorithm in the presence of model uncertainties is to use a learning algorithm. In this work a *gaussian regression* technique is implemented.

Given a reference trajectory in terms of position, $\vec{x}_d$, velocity, $\dot{\vec{x}}_d$, and acceleration, $\ddot{\vec{x}}_d$, and assuming that N consecutive measurements of system inputs and outputs are available, then the regressor algorithm inputs are: (1) the vector, $\vec{\tau}_k$, $k = 1, \ldots, N$, of generalized torques necessary to track the reference trajectory and obtained from the described inverse dynamics (see Sec. 4); (2) the vector of positions, velocities and accelerations, $\vec{p}_k = \{x_e \ y_e \ \dot{x}_e \ \dot{y}_e \ \ddot{x}_e \ \ddot{y}_e\}_k^T$, $k = 1, \ldots, N$, obtained applying the torques, $\vec{\tau}$, to the robot. Indicating with $Z_N = (\vec{p}_k, \vec{\tau}_k)$, $k = 1, \ldots, N$, the regressor is capable to estimate the inverse map $\mu(\vec{p}) : \vec{p} \rightarrow \vec{\tau}$. The unknown $\mu : \mathbb{R}^6 \rightarrow \mathbb{R}^4$ is modeled as realization of a zero-mean gaussian field with covariance $K : \mathbb{R}^6 \times \mathbb{R}^6 \rightarrow \mathbb{R}$. K is assumed to be a gaussian kernel, i.e $K(\vec{p}_i, \vec{p}_j) = e^{-\frac{\|\vec{p}_i - \vec{p}_j\|}{\sigma^2}}$ with $\sigma \in \mathbb{R}_+$. Under the framework of the regularization theory[26], a standard result is the form of the optimal estimate $\hat{\mu}(\vec{p})$, which in this case is given by

$$\hat{\mu}(\vec{p}) = \mathbb{E}\left[\mu(\vec{p})|Z_N\right] = \sum_{i=1}^{N} c_i K(\vec{p}_i, \vec{p}) \tag{12}$$

where $\mathbb{E}[\cdot]$ denotes the expected value, with

$$\begin{bmatrix} c_1 \\ \vdots \\ c_N \end{bmatrix} = (\bar{\mathbf{K}} + \sigma^2 \mathbb{I})^{-1} \begin{bmatrix} \vec{\tau}_1 \\ \vdots \\ \vec{\tau}_N \end{bmatrix} \tag{13}$$

and

$$\bar{\mathbf{K}} = \begin{bmatrix} K(\vec{p}_1, \vec{p}_1) & \ldots & K(\vec{p}_1, \vec{p}_N) \\ \vdots & & \vdots \\ K(\vec{p}_N, \vec{p}_1) & \ldots & K(\vec{p}_N, \vec{p}_N) \end{bmatrix} \tag{14}$$

6. SIMULATIONS AND RESULTS

Dynamic simulations of the manipulator system have been performed with two target trajectories, one linear and one circular. Both control schemes described in Sec. 5 are simulated and their results are compared, also in the presence of inaccurate measurements of the output variables. The results are presented in the following.

In order to accurately simulate the performances of the system, the power supply transfer function is included in the model, thus modifying the input voltages slightly. The power supply considered is a single channel PS375 (Stanford Research Systems, USA).

The trajectories considered in the simulations are traveled with a fifth order polynomial time law which is presented in Fig. 8 (linear trajectory) and in Fig. 11 (circular trajectory). The results of linear trajectory simulations are shown in Fig. 9-10, while those for the circular trajectory are shown in Fig. 12-13.

The comparison of the two control schemes is based on the robustness to output measurements inaccuracies. Such inaccuracies are modeled as uniform noise with an amplitude range of ± 0.01 m. The feedforward compensator performs much better than the PD controller and, therefore, it is more suitable for application to DE systems, whose model is known with non-negligible parameter uncertainties (see Sec. 2). In particular, the maximum position error with FF compensator is roughly half than with PD for both trajectories considered (see Fig. 9b and Fig. 12b). Moreover, the simulations performed including noise show that the system controlled with PD becomes unstable and diverges (results not shown), while the FF compensator is still capable to control the system with some performances degradation. Tab. 1 summarizes the simulations results as absolute position errors and as relative errors w.r.t. the trajectory overall length.

Table 1: Simulations results: absolute error and relative error (w.r.t. trajectory length) for both trajectories and control schemes.

Trajectory	Control	Absolute error [mm]	Relative error [%]
Linear	PD	4.8	5.6%
	FF	1.8	2.1%
	FF w/ noise	8.1	9.5%
Circular	PD	6.7	8.8%
	FF	3.3	4.3%
	FF w/ noise	9.9	12.9%

7. LABORATORY SETUP

The system is designed for space applications and, therefore, it is not expected to be able to withstand the gravity load of ground conditions. A test campaign in a micro-gravity emulating environment is foreseen. The laboratory setup that will be used is a simple passive suspending system, based on high stiffness supports[27]. The manipulator links are suspended by inextensible cables fixed at their center of mass. The cables are vertical and constrain the Z-axis degree of freedom of each link, while they leave the system free to move in the horizontal plane (X-Y). Some perturbations to the X-Y motion are introduced by the suspending system due to a pendulum effect of the cables; in particular, the longer the suspending cables the lower the perturbations. Nevertheless, it is possible to estimate the horizontal forces introduced by the suspending system and design the setup to reduce them within acceptable limits. In the considered case, assuming 3.5 m long cables the maximum perturbing horizontal forces are on the order of 3.5×10^{-2} N equivalent to 7% of F_{max}; the estimated disturbing torques are below 2×10^{-3} Nm equivalent to 7.5% of T_{max}.

Fig. 14 is a schematic view of the proposed test setup. The variables measured in the feedback loop are the end-effector positions, x_e and y_e. A vision system detects the X-Y position of a marker located on the end-effector and determines the control variables through an image processing algorithm, feeding the data to the controller. The control system commands the power supply to provide the correct voltage to the manipulator in order to follow the desired trajectory. The HV power supply circuit needs eight channels to power all the electrodes of two actuators (i.e. two electrode couples per membrane, total four electrode couples per actuator).

8. CONCLUSIONS

In this paper the kinematic, dynamic and control design of a 2-D robotic arm based on DE actuators is presented. This work is a baseline study in the development of a zero-gravity experiment for the performance evaluation of a DE manipulator for space applications. Great potentialities are identified in the implementation of soft robotics technologies to space scenarios.

Two 2-DoF double-cone actuators are assembled in series composing a redundant manipulator with 4 joint variables (two translational and two rotational). Parametric relations developed by the authors are exploited for the assessment of steady state performances (force/torque, stroke/rotation). An approximate dynamic model is developed on the basis of
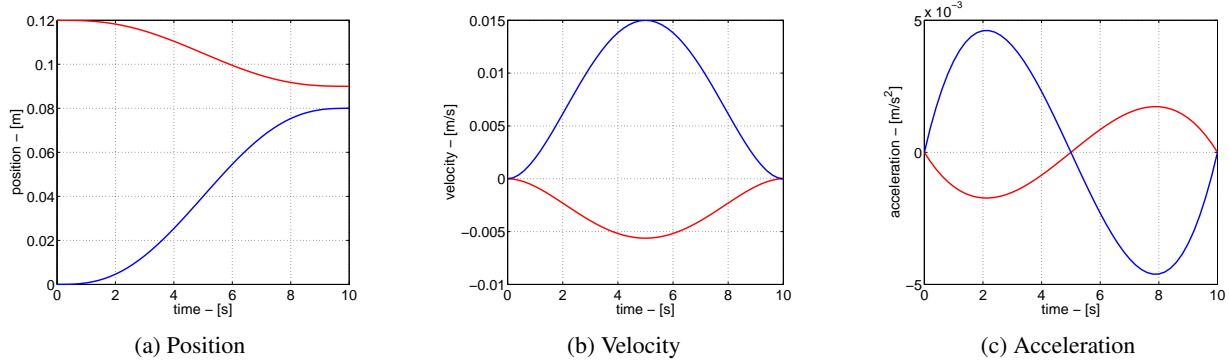
(a) Position   (b) Velocity   (c) Acceleration

Figure 8: Linear trajectory 5th order polynomial time law (X component in red, Y component in blue).

(a) Desired trajectory (black dashed) and actual trajectory (FF in red and PD in blue).   (b) Position error norm.
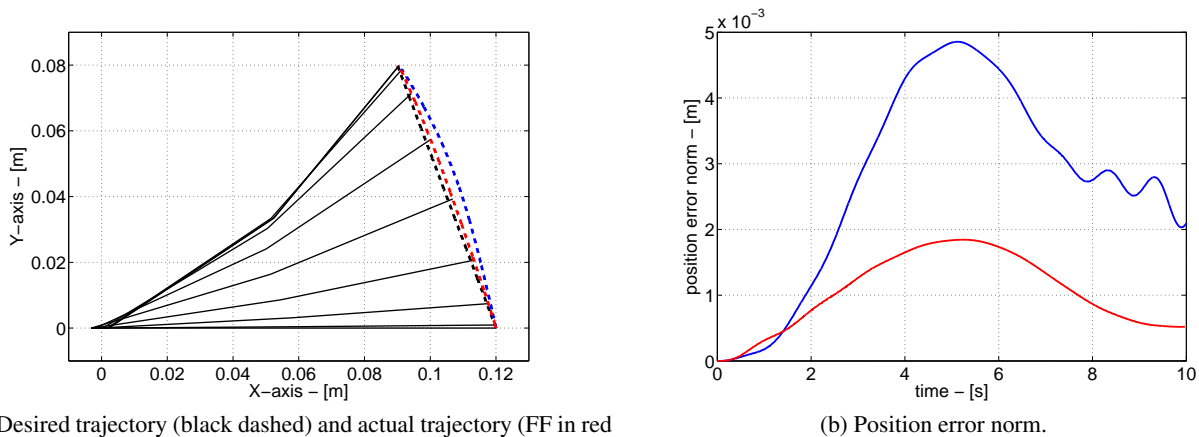
Figure 9: Linear trajectory w/o noise; FF compensator (red) and PD controller (blue).

(a) Desired trajectory (black) and FF compensator actual trajectory (red).   (b) Position error norm.
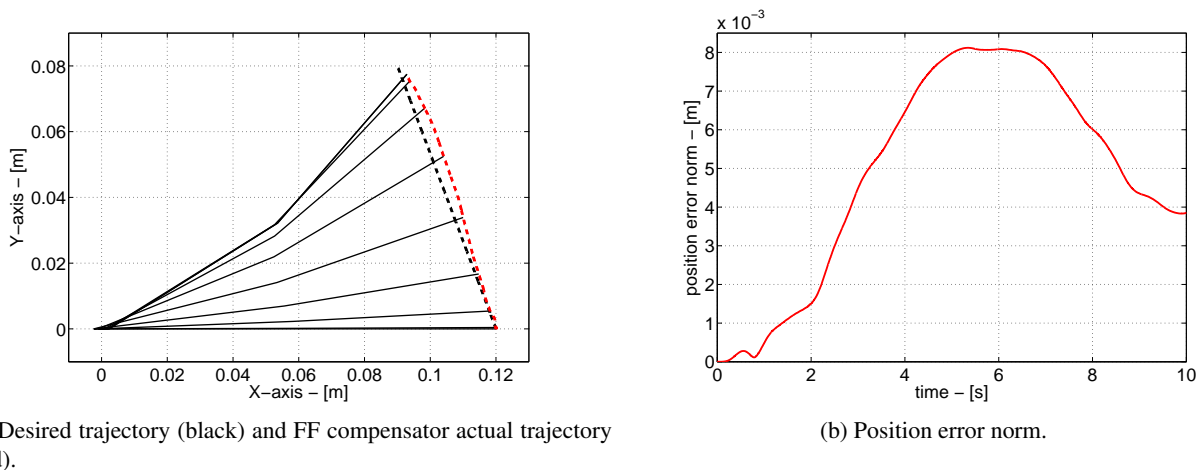
Figure 10: Linear trajectory w/ noise (FF compensator only).

laboratory estimated transfer functions. The manipulator redundancy is exploited to avoid joint limits by minimizing joint variables and, consequently, joint torques and command voltages. The dynamics is inverted with a inertia-weighted version of the Moore-Penrose pseudoinverse and using a torque-based redundancy resolution with decoupling between task space and null space joint torques.

A regressor-based feed-forward controller is developed aiming to a future robust implementation in a laboratory experiment with non-negligible model uncertainties. The performances are compared with those of a classical PD controller
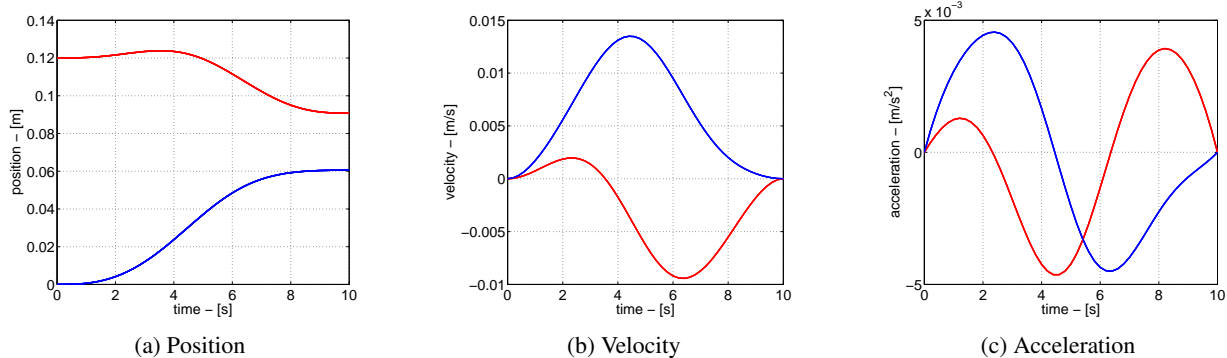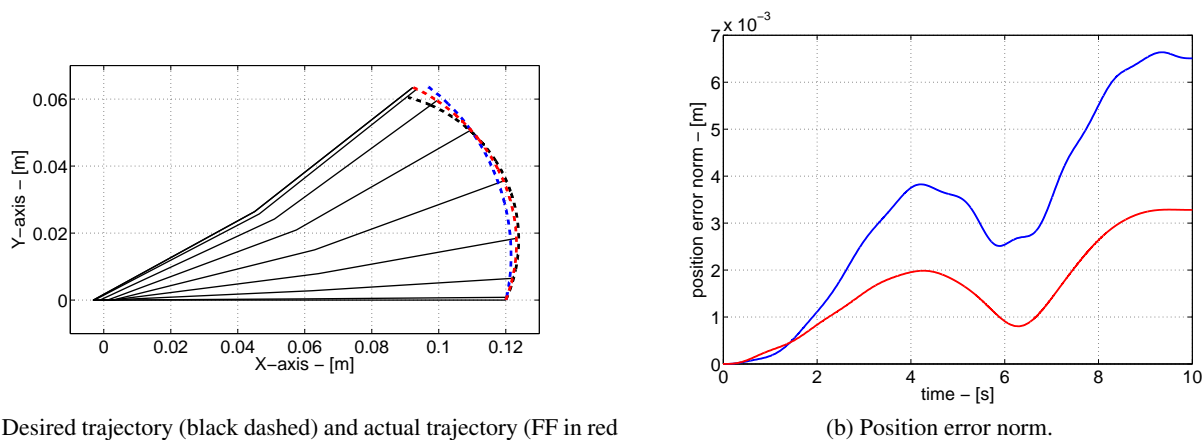
(a) Position   (b) Velocity   (c) Acceleration

Figure 11: Circular trajectory 5th order polynomial time law (X component in red, Y component in blue).

(a) Desired trajectory (black dashed) and actual trajectory (FF in red and PD in blue).

(b) Position error norm.

Figure 12: Circular trajectory w/o noise; FF compensator (red) and PD controller (blue).

(a) Desired trajectory (black) and FF compensator actual trajectory (red).

(b) Position error norm.
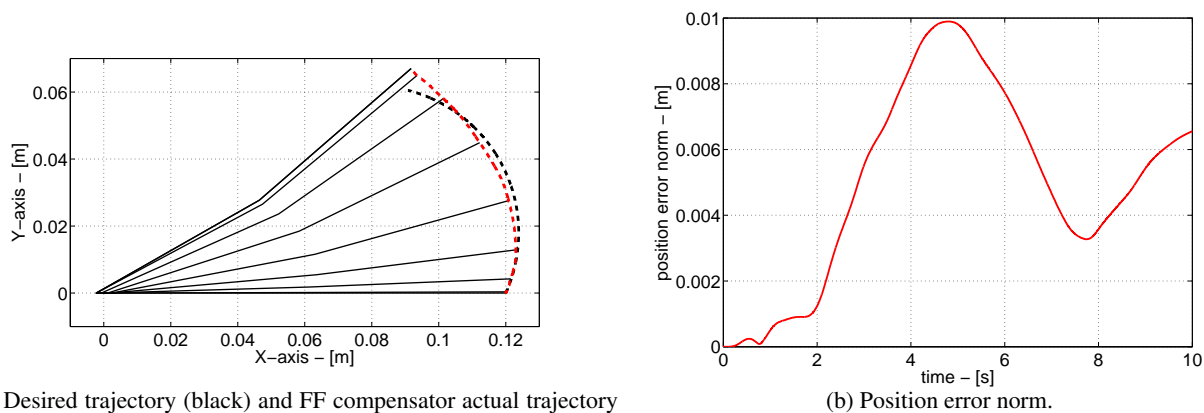
Figure 13: Linear trajectory w/ noise (FF compensator only).

inserting noise on the measured variables. The desired trajectories are followed with a maximum error of 9.9 mm equivalent to 12.9% of the distance traveled by the end-effector. If noise on output is neglected, the trajectories are followed with a maximum error as low as 1.8 mm equivalent to 2.1% of path length.

Finally, a laboratory setup for the micro-gravity simulation based on a rigid suspending system is presented. Since the manipulator operates in the horizontal plane, a good micro-gravity simulation is achievable with some in-plane perturbing loads ($<$ 7.5% of nominal actuator forces/torques).
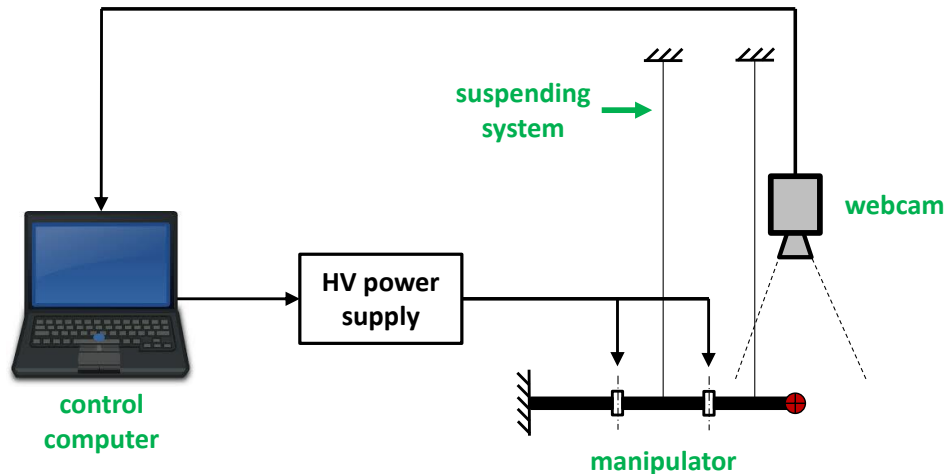
Figure 14: Laboratory setup schematic. All the main components are shown: the manipulator prototype, the suspending system, the vision system sensor (webcam), the control computer and the HV power supply.

REFERENCES

1. Albu-Schäffer, A., Eiberger, O., Grebenstein, M., Haddadin, S., Ott, C., Wimböck, T., Wolf, S., and Hirzinger, G., "Soft robotics," *IEEE Robotics and Automation Magazine* **15**(3), 20–30 (2008).

2. Kim, S., Laschi, C., and Trimmer, B., "Soft robotics: a bioinspired evolution in robotics," *Trends in Biotechnology* **31**(5), 287–294 (2013).

3. Punning, A., Anton, M., Kruusmaa, M., and Aabloo, A., "A biologically inspired ray-like underwater robot with electroactive polymer pectoral fins," in [*Proc. International IEEE Conference on Mechatronics and Robotics*], 241–245 (2004).

4. Conn, A. T. and Rossiter, J., "Antagonistic dielectric elastomer actuator for biologically-inspired robotics," in [*Proc. SPIE Electroactive Polymers and Devices (EAPAD) 2011*], **7287** (2011).

5. Hartl, D. J. and Lagoudas, D. C., "Aerospace applications of shape memory alloys," *Proceedings of the Institution of Mechanical Engineers, Part G: Journal of Aerospace Engineering* **221**(4), 535–552 (2007).

6. Vincenzini, P., Bar-Cohen, Y., and Carpi, F., "Artificial muscle actuators using electroactive polymers," *Trends in Biotechnology* **61**, 180–185 (2008).

7. Fetchko, P., Sellers, J., Spanjers, G., Scherbarth, M., Winters, J., Barrett, R., Lake, M., and Keller, P., "Deployment optimization of a boom for falconsat -3 using elastic memory materials," in [*Proc. 18th Annual AIAA/USU Conference on Small Satellites*], (2004).

8. Bar-Cohen, Y., "Electroactive polymers (eap) as actuators for potential future planetary mechanisms," in [*Proc. NASA/DoD Conference on Evolvable Hardware*], (2004).

9. Kosmas, C., "On-orbit-servicing by hermes on-orbit-servicing system, policy robust planning," in [*Proc. AIAA Space Operations Conference*], **5660** (2006).

10. Izzo, D., Pettazzi, L., and Ayre, M., "Mission concept for autonomous on orbit assembly of a large reflector in space," in [*Proc. 56th International Astronautical Congress*], (2005).

11. Caswell, D., Visentin, G., de Kam, G. O. J., Nugteren, P. R., and Scholten, H., [*ConeXpress Orbital Life Extension Vehicle*], vol. 127, ESA Bulletin (2006).

12. Ogilvie, A., Allport, J., Hannah, M., and Lymer, J., "Autonomous satellite servicing using the orbital express demonstration manipulator system," in [*Proc. International Symposium on Articial Intelligence, Robotics and Automation in Space (i-SAIRAS)*], 77–90 (2008).

13. Oda, M., Kibe, K., and Yamagata, F., "ETS-VII, space robot in-orbit experiment satellite," in [*Proc. IEEE International Conference on Robotics and Automation*], (1).

14. Debus, T. J. and Dougherty, S. P., "Overview and performance of the front-end robotics enabling near-term demonstration (FREND) robotic arm," in [*Proc. AIAA Infotech@Aerospace Conference*], (2009).

15. Uchiyama, M. and Konno, A., "Development of a flexible dual- arm manipulator testbed for space robotics," in [*Proc. IEEE International Workshop on Intelligent Robots and Systems (IROS)*], 375–381 (1990).

16. Pei, Q., Rosenthal, M., Stanford, S., Prahlad, H., and Pelrine, R., "Multiple-degrees-of-freedom electroelastomer roll actuators," *Smart Materials and Strucutres* **13**(5) (2004).

17. Carpi, F., Salaris, C., and Rossi, D. D., "Folded dielectric elastomer actuators," *Smart Materials and Structures* **16**(2) (2007).

18. Anderson, I. A., Tse, T. C. H., Inamura, T., O'Brien, B. M., McKay, T., and Gisby, T., "A soft and dexterous motor," *Applied physics letters* **98** (2011).

19. Conn, A. T. and Rossiter, J., "Towards holonomic electro-elastomer actuators with six degrees of freedom," *Smart Materials and Structures* **21** (2012).

20. Kornbluh, R. D., Pelrine, R., Pei, Q., Heydt, R., Stanford, S., Oh, S., and Eckerle, J., "Electroelastomers: applications of dielectric elastomer transducers for actuation, generation, and smart structures," in [*Proc. SPIE Smart Structures and Materials 2002: Industrial and Commercial Applications of Smart Structures Technologies*], **4698** (2002).

21. Jung, K., Kim, K. J., and Choi, H. R., "A self-sensing dielectric elastomer actuator," *Sensors and Actuators A* **143**, 343–351 (2008).

22. Branz, F., Sansone, F., and Francesconi, A., "Design of an innovative dielectric elastomer actuator for space applications," in [*Proc. SPIE Electroactive Polymer Actuators and Devices (EAPAD) 2014*], **9056** (2014).

23. Siciliano, B., Sciavicco, L., Villani, L., and Oriolo, G., [*Robotics - Modelling, Planning and Control*], Springer (2009).

24. Hu, B., Teo, C. L., and Lee, H. P., "Local optimizationof weighted joint torques for redundant robotic manipulators," *IEEE Transactions on Robotics and Automation* **11**(3), 422–425 (1995).

25. Nakanishi, J., Cory, R., Mistry, M., Peters, J., and Schaa, S., "Comparative experiments on task space control with redundancy resolution," in [*IEEE/RSJ International Conference on Intelligent Robots and Systems*], 3901 – 3908 (2005).

26. Tikhonov, A. and Arsenin, V., [*Solutions of Ill-Posed Problems*], Washington, D.C.: Winston/Wiley (1977).

27. Menon, C., Busolo, S., Cocuzza, S., Aboudan, A., Bulgarelli, A., Bettanini, C., Marchesi, M., and Angrilli, F., "Issues and solutions for testing free-flying robots," *Acta Astronautica* **60**, 957–965 (2007).